



## RESEARCH ARTICLE

# Surface morphology modulation in multilayer scaffolds via ion doping for bone tissue engineering

Paula M. Riosalido<sup>1</sup> | Pablo Velásquez<sup>1</sup>  | Ángel Murciano<sup>2</sup> | Piedad N. De Aza<sup>1</sup> <sup>1</sup>Institute of Bioengineering, Miguel Hernandez University, Elche, Spain<sup>2</sup>Department of Materials, Optical and Electronic Technology, Miguel Hernandez University, Elche, Spain**Correspondence**

Pablo Velásquez, Institute of Bioengineering, Miguel Hernandez University, Avda. Universidad s/n 03202, Elche, Spain.

Email: [pavelasquez@umh.es](mailto:pavelasquez@umh.es)**Editor's Choice**

The Editor-in-Chief recommends this outstanding article.

**Funding information**

MCIN/AEI/10.13039/501100011033 Spain, Grant/Award Number: PID2020-116693RB-C21; Ministerio de Ciencia e Innovación

**Abstract**

This work proposes the use of multilayer scaffolds as a strategy for developing biomimetic structures for bone tissue regeneration. The scaffolds consist of a glass–ceramic core composed of  $\text{CaSiO}_3/\text{Ca}_2\text{P}_6\text{O}_{17}$ , which provides mechanical properties of 2.3 MPa and a total porosity of  $\sim 74\%$ . To modify the surface morphology a double bioactive coating consisting of  $\text{Ca}_3(\text{PO}_4)_2/\text{CaSiO}_3$  doped with  $\text{Na}^+$  and  $\text{K}^+$ , along with varying amounts of  $\text{Mg}^{2+}$  (0–0.75 g  $\text{MgCO}_3$ ) was carried out giving a total porosity of 89.8%. The resulting scaffolds were assessed for in vitro bioactivity according to ISO 23317. After immersion in SBF, the W-05 scaffolds displayed diverse surface morphologies: square HA structure (W-05-3D), hollow HA spheres (W-05-7D) and smooth HA layer (W-05-21D). Cell viability of 3T3 fibroblasts exposed to W-05 scaffolds in direct and indirect assays at concentrations of 15 and 30 mg/mL was assessed according to ISO 10993–5. Initially, cell proliferation decreased compared to controls, but differences became non-statistically significant after 72 h. Hollow spheres (W-05-7D) enhanced cell viability compared to other morphologies and plastic controls. Additionally, degradation products of W-05 stimulated cell division, underscoring scaffold biocompatibility.

**KEYWORDS**

bone tissue engineering, hydroxyapatite, multilayer scaffolds, sol-gel

## 1 | INTRODUCTION

The field of bone tissue engineering (BTE) has significant potential for treating bone injuries and skeletal disorders. Its goal is to achieve effective bone regeneration by combining bioactive scaffolds, osteoprogenitor cells, and growth factors.<sup>1–4</sup>

However, to successfully integrate and support bone regeneration, scaffolds must exhibit characteristics similar to the native bone structure.<sup>5–7</sup> These properties

include surface roughness, interporosity with adequate pore size, biodegradability, suitable mechanical properties and biocompatibility.<sup>4–9</sup> Despite significant progress in this field, critical challenges still remain.

In this sense, ceramic materials are a well-established source of biomaterials for bioengineering applications, particularly in BTE.<sup>3,10–12</sup> They are a promising choice for the design of bone scaffolds due to their biocompatibility, similarity to bone tissue, osteoconductive properties and biodegradability.<sup>9,10</sup> Calcium phosphates (CaP) are

This is an open access article under the terms of the [Creative Commons Attribution-NonCommercial-NoDerivs](https://creativecommons.org/licenses/by-nc-nd/4.0/) License, which permits use and distribution in any medium, provided the original work is properly cited, the use is non-commercial and no modifications or adaptations are made.

© 2024 The Author(s). *Journal of the American Ceramic Society* published by Wiley Periodicals LLC on behalf of American Ceramic Society.

of particular interest as they closely resemble the inorganic component of the bone matrix, both structurally and chemically.<sup>12–14</sup> Within this group, there are two main phases: hydroxyapatite (HA) and  $\beta$ -tricalcium phosphate ( $\beta$ -TCP). These phases are known for their high biocompatibility and in vitro bioactivity.<sup>4,15</sup>

Another family of ceramic materials that has attracted the attention of researchers is calcium silicate minerals.<sup>16,17,19,20</sup> They exhibit excellent bioactivity due to apatite formation and cell proliferation stimulation, in addition to a suitable degradability rate for enabling hard tissue formation.<sup>20–22</sup> Among these materials, wollastonite ( $\text{CaSiO}_3$ ) stands as an interesting biomaterial due to its biocompatibility, biodegradability, and in vitro bioactivity.<sup>18,20,21</sup> However, the practical application of  $\text{CaSiO}_3$  is limited by its inherent brittleness, low mechanical strength, and high ionic dissolution.<sup>18,20</sup>

Another common approach to achieve hard tissue regeneration is the employment of bioactive glasses (BG). These materials typically consist of silicate-, phosphate- or borate- based compositions, often incorporating elements such as sodium and calcium.<sup>23,24</sup> BGs exhibit an excellent bone-bonding ability derived from their well-known bioactivity.<sup>25,26</sup> Furthermore, their biodegradability facilitates material dissolution, yielding products that promote biological regenerative mechanisms including both angiogenesis and osteogenesis.<sup>26,27</sup>

On the basis of the above, the objective of this research is to create scaffolds that imitate the complex function and structure of bone. In this sense, the development of multilayer scaffolds stands as an interesting approach. These scaffolds incorporate several layers of different composition, which remain integrated into a single structure.<sup>28–30</sup> In this manner, each coating can be tailored to offer specific functions and features, such as mechanical support, improved cell adhesion and differentiation, or controlled release of bioactive molecules such as drugs or growth factors. This versatility provides an intriguing opportunity to exploit and combine the properties of different phases typically used in BTE.

The layered structures were specifically designed to fulfil different functions. Wollastonite was chosen as the internal material and template for subsequent layers. A coating of the glassy P6 phase ( $\text{Ca}_2\text{P}_6\text{O}_{17}$ ) was then applied to increase mechanical strength due to its cohesive activity and ability to fill preexisting cracks.<sup>31</sup> The amorphous phase was doped with lithium ( $\text{Li}^+$ ) to improve its mechanical properties.<sup>32</sup> Together, wollastonite and P6 form the ceramic-glass core.

The third layer of the structure contained  $\beta$ -TCP, which functioned as a reservoir for two ions closely linked to bone metabolism: phosphorus ( $\text{PO}_4^{3-}$ ) and calcium ( $\text{Ca}^{2+}$ ).

Wollastonite was chosen as a surface coating to provide silanol groups.<sup>21</sup> To enhance the bioactivity of the system and modify the morphology of the precipitated HA, it was doped with varying amounts of ions related to bone physiology, including sodium ( $\text{Na}^+$ ),<sup>33</sup> potassium ( $\text{K}^+$ ),<sup>34</sup> and magnesium ( $\text{Mg}^{2+}$ ).<sup>35</sup>

## 2 | MATERIALS AND METHODS

### 2.1 | Design and fabrication of multilayer scaffolds

The multilayer scaffolds were obtained by preparing distinct layers using the sol–gel technique. Table 1 summarizes the chemical composition for manufacturing each coating. The initial number indicates the layer sequence, with 1 representing the innermost and 4 the outermost layer, followed by the name of the respective phase. In the case of the fourth layer, the numerical values after W indicate the quantity of magnesium carbonate in grams used to dope the outer layer of wollastonite, being 05 and 075, 0.5 g and 0.75 g of magnesium carbonate respectively.

Sol–gel solutions were formulated using appropriate reactants. Tetraethyl orthosilicate (TEOS, Aldrich 98%); triethyl phosphate (TEP, Aldrich  $\geq 99.8\%$ ); calcium carbonate ( $\text{CaCO}_3$ , Sigma  $\geq 99\%$ ); lithium carbonate ( $\text{Li}_2\text{CO}_3$ , Sigma–Aldrich  $\geq 99\%$ ); sodium carbonate ( $\text{Na}_2\text{CO}_3$ , Sigma  $\geq 99\%$ ); potassium carbonate ( $\text{K}_2\text{CO}_3$ , Sigma  $\geq 99\%$ ); magnesium carbonate ( $\text{MgCO}_3$ , Sigma Aldrich  $\geq 99\%$ ); Ethanol ( $\text{C}_2\text{H}_5\text{OH}$ , Carlo Erba  $\geq 96\%$ ) as solvent and finally hydrochloric acid (HCl 37%, Ensure) as a catalyst.

In all cases, the corresponding compounds were reacted, and the solution's final pH was adjusted to a value between 2 and 3. In order to obtain the first layer, polyurethane sponges with a porosity of 20 ppi (quality materials) were submerged in the sol–gel solution with the 1-W composition, shown in Table 1. After immersion, the samples were dried for 10 min at a temperature of 185°C. The treatment is repeated ten times in order to ensure a uniform coating of the polyurethane sponge. Subsequently, a heat treatment was conducted, comprising a heating ramp of 55 h to reach 1050°C, followed by an 8 h maintenance period before allowing the system to cool to room temperature. Once the initial layer (1-W) has been formed, the second layer (2-P6-Li) of composition shown in Table 1, is obtained using the same methodology described earlier. Lithium is incorporated in a small amount in the formulation to facilitate the melting of the glassy phase. This assembly of the two innermost layers (1-W/2-P6-Li) is referred to as the core scaffold.

The excess of both, lithium and glassy phase of core scaffolds, is eliminated by immersion in 50 mL of the solution

**TABLE 1** Chemical composition of multilayer scaffold coatings.

Layer	Reactives									
	TEOS (mL)	TEP	H <sub>2</sub> O	Ethanol	HCl	CaCO <sub>3</sub> (g)	Li <sub>2</sub> CO <sub>3</sub>	Na <sub>2</sub> CO <sub>3</sub>	K <sub>2</sub> CO <sub>3</sub>	MgCO <sub>3</sub>
1-W	19.28	–	20	5	1	8.62	–	–	–	–
2-P6-Li	–	18.46	20	5	2	3.72	1	–	–	–
3-TCP	–	10.96	20	5	2	9.68	–	–	–	–
4-W-0	19.28	–	20	5	1	8.62	–	0.5	0.5	–
4-W-05	19.28	–	20	5	1	8.62	–	0.5	0.5	0.5
4-W-075	19.28	–	20	5	1	8.62	–	0.5	0.5	0.75

Abbreviations: TEOS, tetraethyl orthosilicate; TEP, triethyl phosphate.

called TRIS, prepared by diluting tris(hydroxymethyl)aminomethane and CaCl<sub>2</sub> in a ratio of 6.5:1 in distilled water to a final volume of 900 mL. The pH was adjusted to between 7.3 and 7.4 using HCl.

The core scaffold, after undergoing chemical etching with TRIS, was coated in accordance with the aforementioned methodology, using the 3-TCP and 4-W (0–0.75) compositions delineated in Table 1. The outermost layers were obtained through a heating ramp of 9 h to reach 1050°C, followed by 8 hours of maintenance before returning to room temperature.

## 2.2 | Materials physicochemical characterization

The cylindrical multilayer scaffolds underwent physicochemical characterization. They measured approximately 11.5 mm in diameter and 9.2 mm in height and weighed  $0.45 \pm 0.09$  g.

### 2.2.1 | Mineralogical characterization: X-ray diffraction

X-ray diffraction patterns were acquired using an automated Bruker-AXS D8 Advance diffractometer employing CuK $\alpha$  radiation (1.54059 Å) to establish the mineralogical composition of the multilayer scaffold. Data collection was carried out following the vertical geometrical Bragg–Brentano ( $\theta/2\theta$ ) configuration in plane reflection mode between 5° and 55° ( $2\theta$ ). The measurement steps were carried out in increments of 0.05°, with a duration of 5 s, while the X-ray tube was operated at 40 kV and 30 mA. The resulting diffractograms were compared to those in the Crystallography Open Database (COD) using Power Diffraction Match! version 3.16 Build 288 software.

### 2.2.2 | Physical evaluation

#### *FESEM-EDX microstructure analysis*

The microstructure's morphology and composition were analyzed using a field emission scanning electron microscope (FESEM, ZEISS SIGMA 300 VP) coupled with energy dispersive X-ray spectroscopy (EDX, ZEISS Smart-EDX). All samples were palladium coated prior to analysis.

#### *Mechanical compressive strength test*

To test the scaffold's compressive strength, scaffolds were subjected to a compression test using a simple manual test stand (SVL-1000 N, IMADA).

#### *Porosity study*

An exhaustive analysis of pore distribution and porosity (< 300  $\mu$ m) was undertaken through the mercury porosimetry technique. A Poromaster 60 GT device manufactured by Quantachrome Instruments was used for this purpose, operating within a pressure range of 0.927–35248.6 psi. Porosity associated with pore sizes exceeding 300  $\mu$ m was determined using a pycnometer filled with water, followed by the application of Archimedes' principle.

## 2.3 | In vitro bioactivity evaluation

In vitro bioactivity assays were conducted according to ISO/FDIS 23317 standard guidelines.<sup>36</sup> The scaffolds were immersed in 50 mL of simulated body fluid (SBF) and kept at  $37 \pm 0.5^\circ\text{C}$  in a water bath with agitation for 1, 3, 7, 14, and 21 days. After drying the samples, FESEM-EDX was used to search and identify precipitates on the scaffold surfaces.

The SBF was analyzed using inductively coupled plasma optical emission spectrometry (ICP-OES, Perkin-Elmer Optima 2000™) to monitor changes in elemental concentrations.

## 2.4 | In vitro biological evaluation

The response of the W-05 scaffold to cells in vitro was evaluated according to ISO 10993–5 standards.<sup>37</sup> The study examined the direct effect of the W-05 scaffold on 3T3 murine embryonic fibroblasts before and after SBF exposure, as well as the indirect impact on cells mediated by its dissolution products (DP).

The 3T3 fibroblast cells were cultured in Petri dishes Dulbecco's modified Eagle medium (DMEM—Gibco) supplemented with 10% fetal bovine serum (FBS—Corning) and 1% penicillin/streptomycin (PS—Gibco) and incubated at 37°C in a humidified atmosphere with 5% CO<sub>2</sub>. The cell culture medium was refreshed every 48 hours and subcultured when 80% confluence was reached.

### 2.4.1 | Direct cell culture

The study analyzed the cytotoxicity of the W-05 scaffold and the impact of its surface morphology on cells. Cell proliferation was compared across different scaffold topographies, including the scaffold without SBF (W-05-0D), the square morphology after 3 days of SBF exposure (W-05-3D), the hollow spheres on day 7 (W-05-7D), and the regular surface on day 21 (W-05-21D). The control group consisted of cells seeded on plastic. Before starting the assays, the scaffolds were sterilized by exposing each side of the structure to UV light for 4 h.

Then, the scaffolds underwent a pretreatment procedure to achieve surface wetting, allowing for protein adsorption and subsequent cell adhesion. The procedure involved completely covering the scaffold surface with culture medium supplemented with 10% FBS and incubating for 30 min at 37°C under a 5% CO<sub>2</sub> atmosphere. 24-well plates were used in this case due to the dimensions of the scaffold. After the incubation period, the culture medium was removed, and the cell seeding process began. Exactly 50,000 cells were seeded onto each scaffold in a 25 µm droplet, positioned at the central region of the scaffold surface to minimize cell adhesion to the plastic substrate of the well plate. The cells adhered for 30 min at 37°C with 5% CO<sub>2</sub>. Culture medium was added to each well, ensuring complete coverage of the scaffold. The samples were incubated with cells for 24, 48, and 72 h.

Cell viability was assessed using the colorimetric viability 3-[4,5-dimethyl-2-thiazolyl]-2,5-diphenyltetrazolium bromide or MTT assay from Sigma-Aldrich.

The Microplate Reader RT-2100C (Neuvar Inc.) was used to obtain absorbance readings at 570 nm, following the manufacturer's instructions.

After each assay interval, the culture medium was removed. The scaffolds were then transferred to a new 24-well plate to exclude cells attached to the bottom of the well and not to the scaffold. As the scaffolds could not fit in the plate reader, 200 µL from each well were transferred to a 96-well plate, and the absorbance was measured at 570 nm.

### 2.4.2 | Indirect cell culture

To investigate the impact of ions released by the W-05 scaffold on cells, samples were incubated in DMEM supplemented with 10% FBS and 1% PS. After sterilization, the scaffolds were weighed, and two dilutions were made, always ensuring complete coverage of the sample. For the first dilution, 1 mL of culture medium was added for every 15 g of scaffold, while for the second dilution, 1 mL was added for every 30 g. Samples were incubated for 1, 3, and 7 days.

To study the effect of DP on cells, 96-well plates were seeded with a density of 15,000 cells/cm<sup>2</sup>, 24 hours before the experiment to allow cell adherence. The culture medium was then replaced with conditioned medium, except for the control wells where fresh, unconditioned culture medium was added. The cells were incubated for 24, 48, and 72 h and MTT assay was performed.

## 2.5 | Statistical analysis

At each designated time point of the study, between-group comparisons were conducted using one-way analysis of variance (one-way ANOVA), followed by multiple comparisons using Tukey's test. Differences among groups were assessed for statistical significance using a predetermined alpha threshold of 0.05 and a 95% confidence level. Data are presented as mean ± SD. All statistical analyses were performed using GraphPad 8.0 software.

## 3 | RESULTS

### 3.1 | Physicochemical characterization of the core

The scaffolds were obtained through the creation of a glass-ceramic core, followed by the application of a double bioactive coating.

The experimental diffractograms of the W-P6-Li core before and after TRIS chemical etching are displayed in Figure 1A. The core scaffolds (W-P6-Li) were composed of cristobalite-SiO<sub>2</sub> (COD 96-900-8225) and calcium diphosphate-Ca<sub>2</sub>P<sub>2</sub>O<sub>7</sub> (COD 96-100-1557) as major



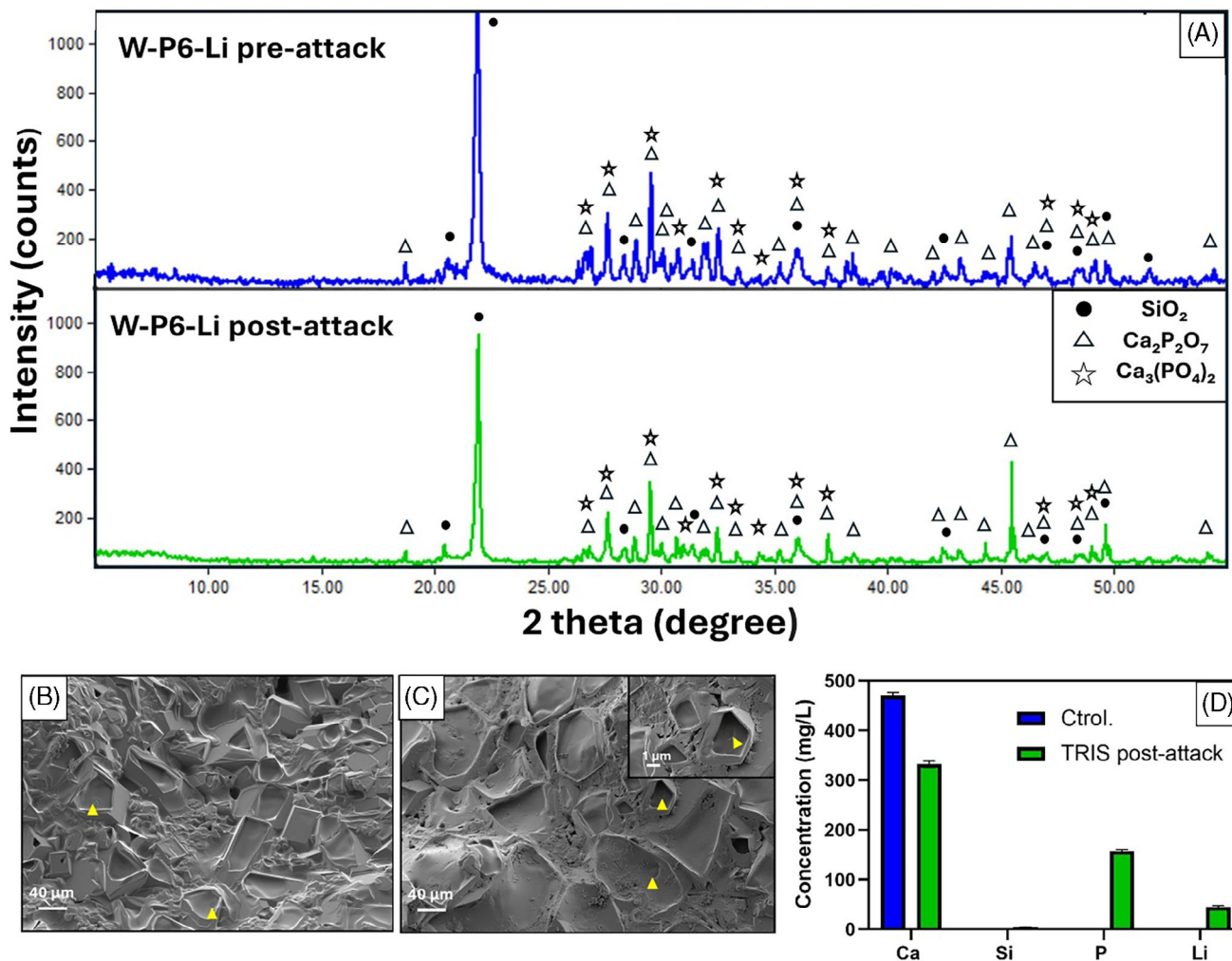


**FIGURE 1** The effect of TRIS etching on the W-P6-Li core was characterized by X-ray diffraction (XRD) (A), field emission scanning electron microscope (FESEM)–energy dispersive X-ray spectroscopy (EDX) before (B), and after (C) treatment and inductively coupled plasma optical emission spectrometry (ICP-OES) (D).

crystalline phases, as well as a residual amount of  $\beta$ -TCP- $\text{Ca}_3(\text{PO}_4)_2$  (COD 96-151-7239) before TRIS exposure. These phases were also found in W-P6-Li attacked scaffolds. However, TRIS-etching resulted in a slight decrease in background at low  $2\theta$  angles.

To confirm the presence of the glassy phase visually, the sample underwent FESEM-EDX scanning (Figure 1B,C). Upon comparing the core's microstructure before and after the attack, it is evident that the core initially displayed large crystals that were covered by an amorphous phase (Figure 1B). However, after the TRIS treatment, the surface glassy phase decreased significantly (Figure 1C). Elemental analysis showed that this vitreous phase consisted mainly of Si and P with a low Ca content (Table S1 and Figure S1). Although the proportion of P and Si varied considerably, the Ca/P + Si ratio remained within the range of 0.015–0.018. However, large crystals were deficient in Si and showed a decreasing Ca/P ratio from the

center (1.43–1.55) to the crystal boundary (0.93–1.14). On closer examination of the crystals, a small central grain (▲) composed of Si and poor in Ca can be seen. Additionally, precipitation of Ca-rich grains was observed following chemical etching.

The chemical treatment resulted in an increase in the concentration of P, Li, and Si in the TRIS solution, presumably from the core scaffolds. However, a decrease in Ca concentration was observed (Figure 1D).

### 3.2 | Physicochemical characterization of the scaffolds

As for the mineralogical characterization, the experimental XRD spectra (Figure 2) confirmed the presence of some of the formulated phases: wollastonite (◇) (COD 96-900-5779) and  $\beta$ -TCP (☆) (COD 96-151-7239). However, the new

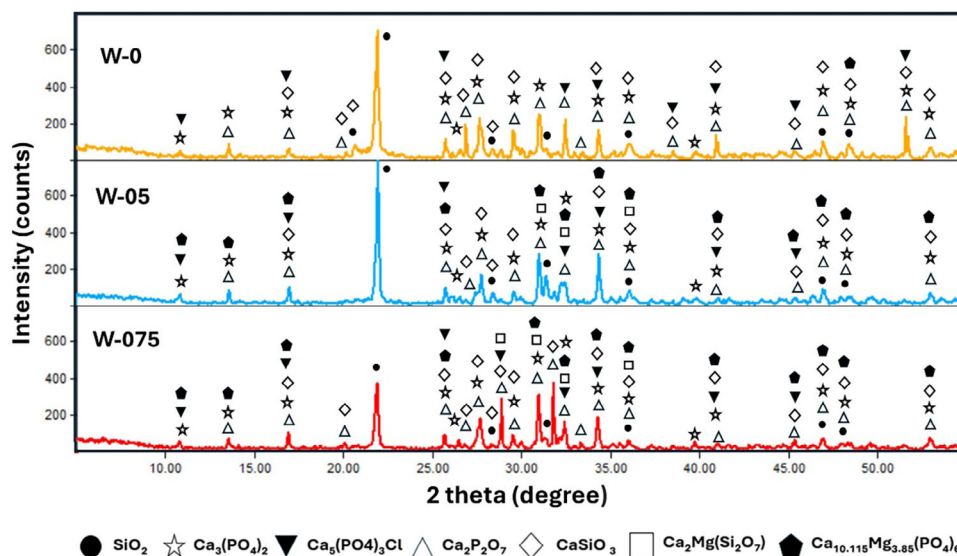


FIGURE 2 X-ray diffraction (XRD) spectra of overall scaffolds W-0, W-05, and W-075.

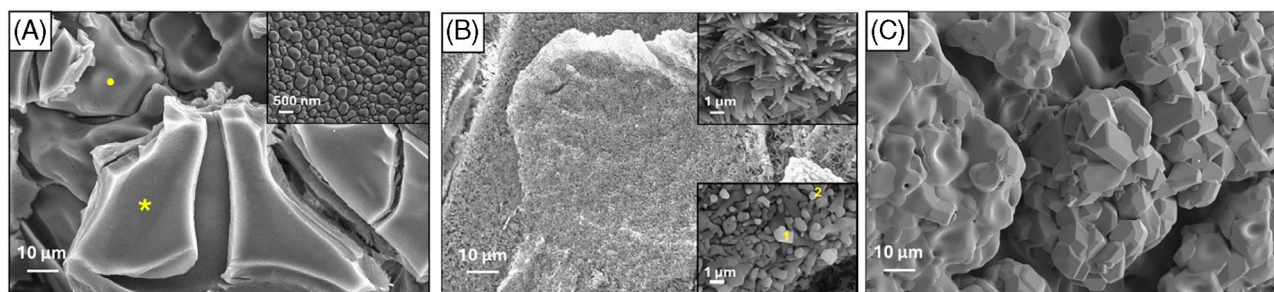


FIGURE 3 Field emission scanning electron microscope (FESEM) micrographs of the microstructure of scaffolds W-0 (A), W-05 (B), and W-075 (C).

crystalline phases were detected in the three scaffolds, including chlorapatites- $\text{Ca}_5(\text{PO}_4)_3\text{Cl}$  ( $\blacktriangledown$ ) (COD 96-210-5266), as well as cristobalite ( $\bullet$ ) (COD 96-900-8225) and calcium diphosphate ( $\triangle$ ) (COD 96-100-1557), which were previously found in the core (Figure 1A). In addition, Mg-rich compounds were identified in W-05 and W-075 scaffolds. These phases were whitlockite- $\text{Ca}_{10.115}\text{Mg}_{3.85}(\text{PO}_4)_6$  ( $\blacklozenge$ ) (COD 96-901-2137), a non-stoichiometric, Mg-rich phase derived from  $\beta$ -TCP, and akermanite- $\text{Ca}_2\text{MgSi}_2\text{O}_7$  ( $\square$ ), (COD 96-900-6942).

Figure 3 displays the microstructure analysis of the scaffolds W-0, W-05 and W-075 using FESEM-EDX. Sample W-0 (Figure 3A) outlines the deposition of two distinguishable layers: 3-TCP ( $\bullet$ ) and 4-W-0 ( $\ast$ ). Although the surface of 4-W-0 appears smooth, enlarged images reveal rounded structures composed mainly of Ca and Si in a ratio of 0.55 to 0.75, as indicated by the EDX spectra (Table S2 and Figure S2). However, the surface of the W-05 scaffold exhibited various regular structures (Figure 3B). The ele-

mental composition analysis revealed that grains XI and XII (see figure), were rich in calcium, silicon, and phosphorus. The Ca/P ratios were 2.63 and 4.48, the Ca/Si ratios were 3.47 and 2.36, and the Ca/P + Si ratios were 1.49 and 1.54, respectively. However, the elongated structures contained only Ca and Si in a ratio of 2.06–2.13. Regarding W-075 scaffold, the surface was homogeneously covered by polygonal CaP crystals. The Ca/P ratio ranged from 1.44 to 1.47 in the central zone and 1.35–1.37 at the edge.

With regard to the analysis of porosity, Figure 4A illustrates a representative scaffold of all the samples employed for the mercury porosimetry tests, which exhibits interconnected open porosity. The analysis of the W-P6-Li, W-0 and W-05 samples revealed similar pores characteristics, with two distinct regions (Figure 4B). The W-0 scaffolds mainly exhibited interparticle porosity, with an approximate pore diameter of 230–1.3  $\mu\text{m}$ , and to a lesser extent intra-particle pores between 0.45 and 0.01  $\mu\text{m}$ . Similarly, the porosity of the W-05 samples was mainly interparticle, with pore

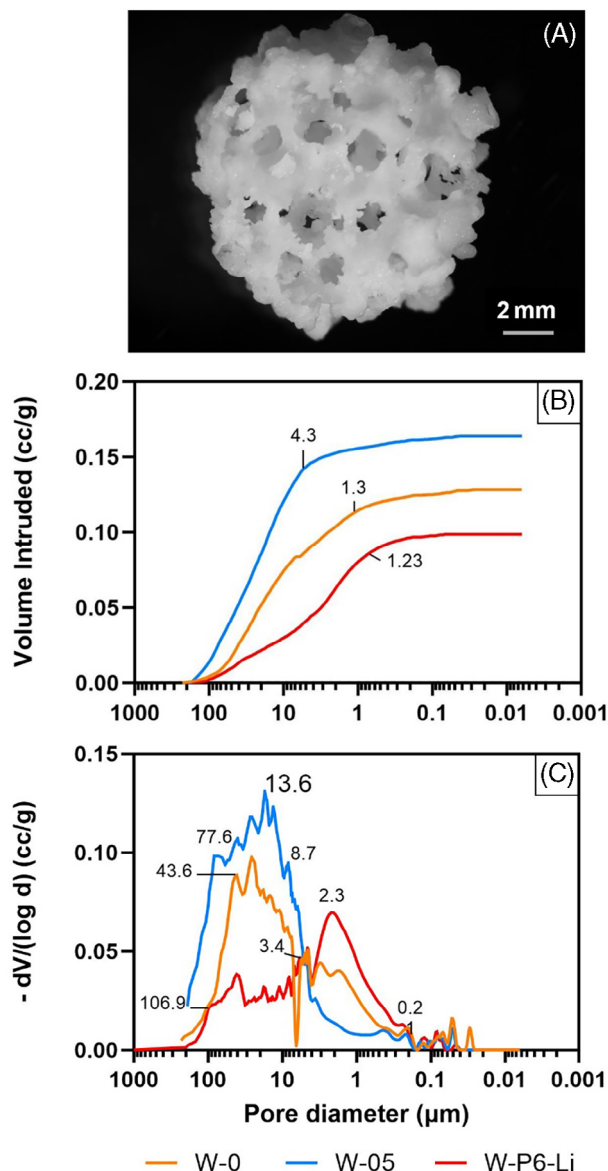


**FIGURE 4** Representative optical image of the scaffolds (A) and curves derived from the mercury porosimetry technique: (B) cumulative, and (C) differential intrusion volume versus pore diameter.

diameters ranging from 190 to 4.3  $\mu\text{m}$ . Intraparticle pores varied between 0.79 and 0.05  $\mu\text{m}$ . Although the interparticle pore sizes of the core, W-P6-Li, were similar to those of samples W-0 and W-05 (199–1.23  $\mu\text{m}$ ), the abundance was notably lower. This is reflected by a decrease in the volume of intruded mercury. Figure 4B shows that the W-0 and W-05 scaffolds have the majority of pores in the range of 150 to 7  $\mu\text{m}$ . However, the core exhibits a wider and more homogeneous range, with the main peak at 2.3  $\mu\text{m}$ , shifted to the right compared to that of the W-0 and W-05 scaffolds. Additionally, all three samples exhibit pores below 100 nm.

Table 2 summarizes the physical properties of the scaffolds, including the compression test results which

provided additional insights into the porosity results due to their inverse relationship.

Scaffold W-075 exhibited physical properties similar to those of scaffold W-05, indicating that the additional 0.25 g  $\text{MgCO}_3$  did not have a significant impact.

### 3.3 | In vitro bioactivity evaluation

Regarding the bioactivity assays, the FESEM–EDX scanning revealed significant changes in surface morphology of the samples (Figure 5). Scaffold W-0, initially showed a Ca-Si precipitate resembling tangles with a ratio of 0.56–0.61 (Table S3 and Figure S3). A residual amount of P was also present, resulting in a Ca/P + Si ratio of about 0.5. After 3 days, the precipitate adopted an elongated morphology with a higher P content than the previous precipitate, resulting in a Ca/P ratio of 4.65–4.74, Ca/Si of 1.24–1.5 and Ca/P + Si of 0.98. However, after 1 week, the precipitate assumed a morphology very similar to that of HA and was composed mainly of Ca and P, with a Ca/P of 1.64–1.68, Ca/Si of 1.31–1.53 and Ca/P + Si of 24.08–25.7. After 2 weeks, the surface still showed apatite-type precipitates, although in some areas they had begun to dissolve. Elemental analysis showed that the precipitate was rich in silicon, calcium and phosphorus. The Ca/P ratios were 2.35–2.47, Ca/Si 8.17–9.4 and Ca/P + Si 1.76–1.81. On Day 21, polygonal grains of calcium and phosphorus were identified with a Ca/P ratio of 1.43–1.57 in the central region and 1.03–1.21 at the edge. There was also a rounded calcium–silicon phase with a Ca/Si ratio of 0.47–0.7.

Scaffold W-05 displayed a precipitate from the first day of immersion in SBF, which gradually accumulated as the immersion time increased. The precipitate underwent significant morphological changes, initially forming tangles, adopting a square shape after 3 days, and evolving into spheres on the seventh day. These spheres, consisting of thin needles, persisted until day 14 before coalescing and disappearing on day 21. EDX analyses showed Ca/P ratios of 1.32–1.35 on Day 1, 1.6–1.75 on Day 3, 1.54–1.6 on Day 7, 1.6–1.69 and 1.53–1.6 on Day 21. It should be noted that although the precipitates did not contain significant amounts of Si on Days 1, 7, 14 and 21, a high Si content was detected on Day 3. This resulted in a Ca/Si ratio of 2–2.5 and a Ca/P + Si ratio of 0.88–1.03.

With regards to W-075 scaffold, small spherical precipitates appeared after one day of immersion in SBF. The elemental analysis revealed high levels of Ca, Si, and P, with the following ratios: Ca/Si of 1.22–1.73, Ca/P of 1.46–1.53, and a Ca/P + Si ratio of 0.53–0.81. After 3 days, the spherical precipitates were evenly distributed across the surface, with an almost unchanged Ca/P ratio of 1.51–1.53, as well as a Ca/Si of 3.19–3.81 and Ca/P + Si of 1.03–1.1.



TABLE 2 Porosity and compressive strength of the core (W-P6-Li) and the overall W-0 and W-05 scaffolds.

Sample	Intraparticle Porosity* (%)	Interparticle Porosity*	Porosity (< 300 $\mu\text{m}$ )*	Porosity (> 300 $\mu\text{m}$ )**	Compressive Strength*** (MPa)
W-P6-Li	11.38	9.38	$20.8 \pm 0.1$	$74.5 \pm 0.1$	$2.3 \pm 0.5$
W-0	7.47	18.11	$25.6 \pm 0.1$	$87.6 \pm 0.1$	$1.9 \pm 0.3$
W-05	3.24	27.13	$30.4 \pm 0.1$	$89.8 \pm 0.1$	$1.8 \pm 0.6$

\*Hg Porosimetry Technique.

\*\*Picnometry.

\*\*\*Simple Manual Test Stand.

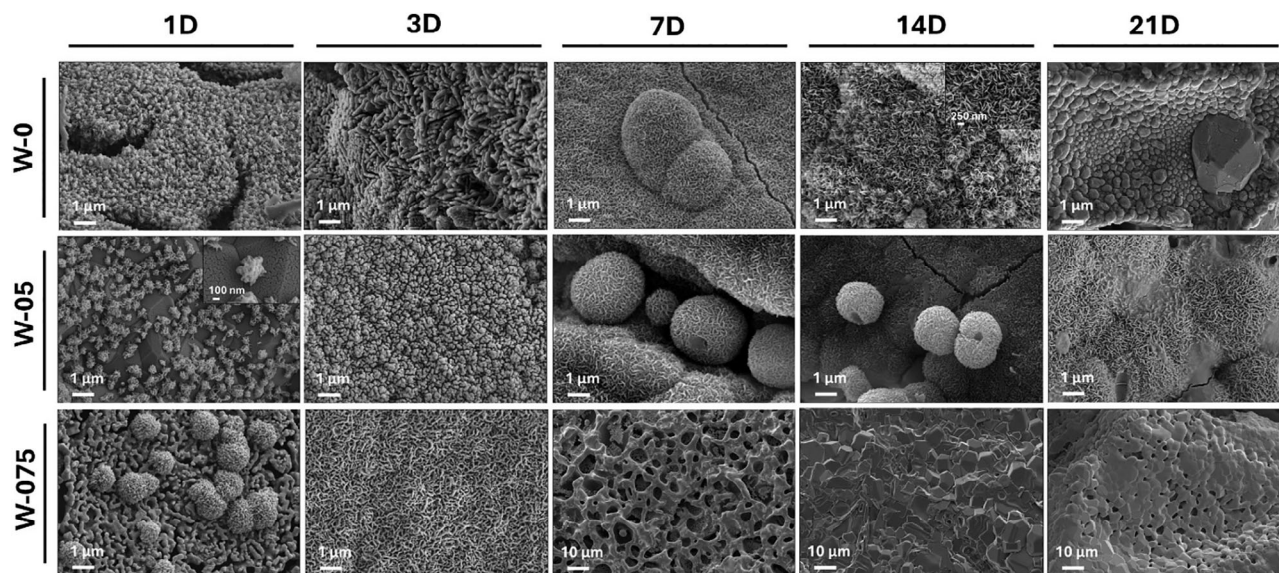


FIGURE 5 Scanning electron microscope (SEM) micrographs of W-0, W-05 and W-075 scaffolds after 1, 3, 7, 14 and 21 days of immersion in simulated body fluid (SBF).

However, the precipitate disappeared completely after 7 days, revealing a ring-shaped microstructure based on calcium and phosphorus in a ratio of 1.43–1.5. After 14 days in SBF, no precipitates were observed, only calcium phosphate crystals, with a Ca/P ratio of 1.29–1.33 in the central part and of 1.01–1.19 in the peripheral part. Finally, after 21 days of immersion, calcium phosphate crystals were again identified, but in this case with a higher calcium content, resulting in a Ca/P ratio of 1.62–1.86.

The variation of Si, Ca, P, Li and Mg was monitored by ICP-OES throughout the 21-day test to complement the bioactivity studies. Figure 6 displays the curves obtained for each scaffold. The results indicate that when the sample is bioactive and has a CaP precipitate, there is a decrease in the concentration of P in the SBF. Conversely, when the sample loses bioactivity, the P concentration in the SBF increases.

While samples W-0 and W-05 show almost no changes in lithium concentration, a noticeable oscillating behaviour of Li is observed in the W-075 scaffold.

Specifically, the concentration in SBF increases from Days 7 to 14 before falling again on Day 21.

### 3.4 | In vitro biological evaluation

The W-05 scaffold was chosen for in vitro cellular assays as the primary aim of this research is to modulate the surface morphology of scaffolds to enhance their biological properties. According to the in vitro bioactivity results, this scaffold displayed hollow HA-like spheres, making it a potential controlled release agent.

The study investigated the impact of W-05 scaffold surface morphology on cell proliferation before (Figure 3B) and after SBF exposure (Figure 5-3D, 7D, 21D), in addition to assessing cytotoxicity.

Regarding the direct assay (Figure 7A), a decrease in cell viability was observed in all scaffold types after 24 h of treatment when compared to the control group. This difference was particularly noticeable in W-05-3D



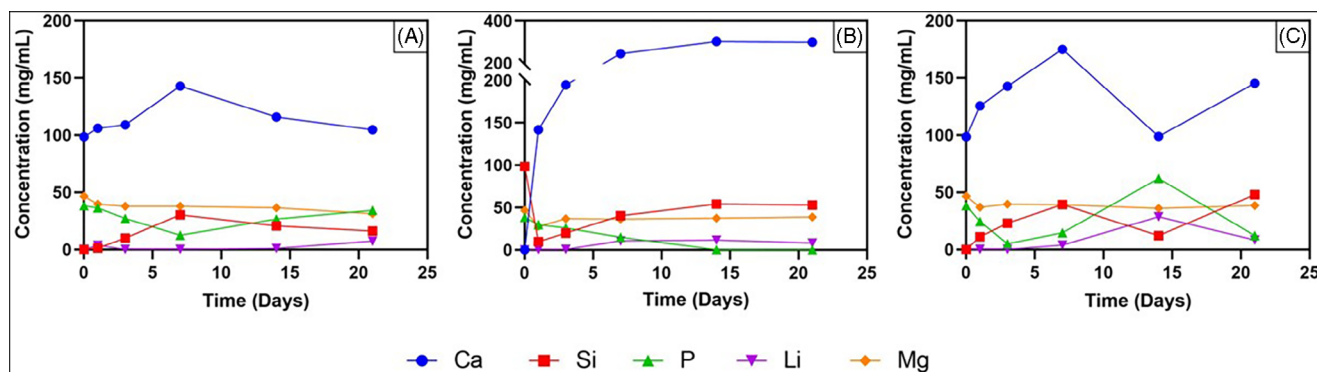


FIGURE 6 Changes in the concentration of Ca, Si, P, Li and Mg in simulated body fluid (SBF) as the immersion time of scaffolds W-0 (A), W-05 (B), and W-075 (C) in SBF increases.

and W-05-21D, although it was also observed in W-05-0D and W-05-7D. After 48 h, the differences were no longer statistically significant for the W-05-7D scaffold, while they persisted for W-05-0D, W-05-3D, and W-05-21D. Furthermore, W-05-7D exhibited increased cell proliferation compared to W-05-0D and W-05-21D. After 72 h of incubation, W-05-7D showed an increase in cell viability compared to W-05-21D. It is important to note that both control and scaffold-exposed wells showed a general growth trend over time.

Figure 7B,C shows the viability of cells incubated with the different DPs. The MTT assay results for the 15 mg/mL concentration (Figure 1B) showed a significant increase in cell proliferation in cells incubated with conditioned medium compared to the control, particularly for DP-3D and DP-7D, although to a lesser extent also for DP-1D. These differences persisted throughout the study. Similarly, DP at 30 mg/mL (Figure 7C) induced higher cell viability compared to cells incubated in plastic, again particularly for DP-3D and DP-7D.

## 4 | DISCUSSION

In this study, three types of multilayer 3D porous ceramic scaffolds with different surface morphologies were fabricated using the sol-gel method. It is challenging to find a single material that can mimic all the characteristics of the bone extracellular matrix.<sup>38</sup> Recognizing the versatility of the sol-gel method, which offers the possibility of depositing coatings on other materials,<sup>39</sup> multilayer scaffolds have been developed in this research. This has enabled the creation of novel and more biomimetic structures for potential clinical applications.

Four different coatings, each with a specific function, were applied to a polyurethane sponge template using the polymer sponge replication technique. The first step was to synthesize the ceramic-glass core W-P6-Li, followed by

chemical etching with TRIS solution, to remove the excess glassy phase.

On the basis of XRD results, it was found that the W-P6-Li core is primarily composed of silicon dioxide and calcium pyrophosphate crystalline phases, with a residual amount of  $\beta$ -TCP (Figure 1A). These phases were likely formed through ionic migration during the sintering treatment from the innermost layer of wollastonite to the following layer, P6-Li.

This migration is attributed to  $\text{Ca}_2\text{P}_6\text{O}_{17}$ , a calcium ultraphosphate comprising layers of rings of six phosphorus atoms bonded through oxygen atoms. The negative charge from the phosphorus atoms is balanced by two calcium atoms.<sup>40</sup> The structure is characterized by high energy, which it is able to reduce by capturing calcium and breaking the rings. The phase obtained by this process is  $\text{Ca}_2\text{P}_2\text{O}_7$ . In the presence of an adequate calcium concentration, calcium pyrophosphate can be formed. In this instance, the 1-W wollastonite serves as a source of calcium, facilitating the transformation of ultraphosphate to pyrophosphate. Consequently, the wollastonite undergoes a transformation, adopting the form of  $\text{SiO}_2$  (Figure 1A,B), a calcium-free phase. FESEM-EDX analysis of the core (Table S1) corroborated these data. Crystals found in the core, had a Ca/P ratio of about 1.5 within the central region, consistent with  $\beta$ -TCP. Additionally, the Ca/P ratio decreased to approximately 1 at the edge, which coincides with the Ca/P of calcium pyrophosphate. Upon closer inspection of the crystals, a small central grain ( $\blacktriangle$ ) that is rich in Si and poor in Ca is visible, indicating the presence of  $\text{SiO}_2$ . Based on these data, it can be inferred that the  $\text{SiO}_2$  grain was most likely wollastonite. However, after releasing  $\text{Ca}^{2+}$  ions to the surrounding glassy phase, it remains as  $\text{SiO}_2$ . Consequently, the nearby zones will receive a greater calcium contribution, promoting the formation of  $\beta$ -TCP. Meanwhile, the distant regions, such as grain boundaries, will be forced to form another stable phase with a lower calcium content, namely calcium pyrophosphate.

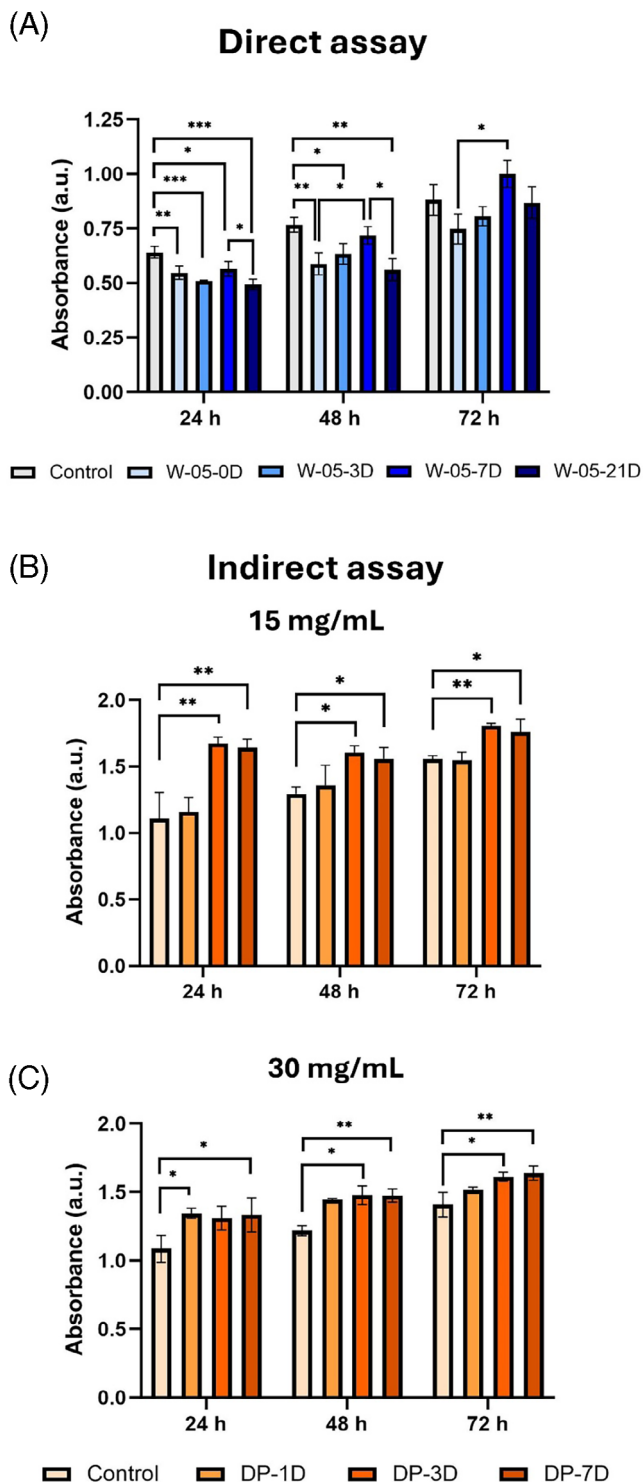


FIGURE 7 Cell viability study of 3T3 cells directly exposed to the different surface morphologies displayed by the W-05 scaffold (A) or to its dissolution products, at a concentration of 15 mg/mL (B) or 30 mg/mL (C). Data were shown as means  $\pm$  SD.  $N = 3$ , \*  $p < 0.05$ , \*\*  $p < 0.01$ , \*\*\* =  $p < 0.001$ .

All these crystals are surrounded by a glassy phase which, in addition to matching the elemental composition of 2-P6-Li, was rich in Si. This is probably a consequence of the wollastonite transformation in which some of the Si migrates into the glassy phase and changes its composition. Although the glassy phases do not produce characteristic peaks to identify them, the low  $2\theta$  region in the XRD pattern is sensitive to amorphous phases and can manifest itself as increased background, as observed in Figure 1A.

The core was then subjected to a chemical attack with TRIS to remove the excess vitreous phase. The attack was characterized by ICP-OES (Figure 1D), which indicated the liberation of P, Li, and Si. This suggests the hydrolysis of P6-Li. XRD validated this elimination by showing a reduction in background in the amorphous region (Figure 1A). This was also visually verified by FESEM-EDX (Figure 1C). Although there is evidence of calcium migration into the sample, the amount is negligible and does not affect the mineralogical composition.

W-0, W-05 and W-075 scaffolds shared most of the phases (Figure 2). Among them,  $\text{SiO}_2$  and  $\text{Ca}_2\text{P}_2\text{O}_7$  were formed through ion migration, while the  $\text{Ca}_5(\text{PO}_4)_3\text{Cl}$  crystals likely originated from the HCl catalyst used during synthesis. Furthermore, the phases  $\text{Ca}_3(\text{PO}_4)_2$  and  $\text{CaSiO}_3$  were also detected. The W-05 and W-075 samples contained two extra phases: akermanite ( $\text{Ca}_2\text{MgSi}_2\text{O}_7$ ), a bioceramic with excellent bioactivity and degradation rates that is known for its osteoinductive properties,<sup>41,42</sup> and whitlockite, a non-stoichiometric phase derived from  $\beta$ -TCP that is rich in magnesium ( $\text{Ca}_{10.115}\text{Mg}_{0.385}(\text{PO}_4)_6$ ). This is an interesting finding considering that whitlockite consolidates as the second most abundant inorganic phase in bone, after HA.<sup>43,44</sup> It stands out for its biocompatibility and superior osteogenic properties compared to  $\beta$ -TCP and HA.<sup>44,45</sup> For this reason, it has been the subject of much research in recent years.<sup>44–46</sup>

FESEM-EDX scanning of the scaffolds revealed that even small variations in the amount of dopant Mg in the wollastonite coating produced significant microstructural changes (Figure 3). The presence of surface calcium phosphates was found to be directly correlated with the amount of Mg used as a dopant, showing a proportional relationship. A plausible explanation is that Mg serves to compensate for the calcium deficit resulting from ionic interlayer migration. This phenomenon could also explain the presence of whitlockite, in the XRD spectra of samples W-05 and W-075 (Figure 2).  $\beta$ -TCP could compensate for its loss of  $\text{Ca}^{2+}$  by sequestering  $\text{Ca}^{2+}$  or  $\text{Mg}^{2+}$  from the surface wollastonite, resulting in the formation of whitlockite.

Mechanical compatibility between implants and bone is an important consideration. Trabecular bone strength varies with age and anatomical region, with compressive

strength previously measured between 1.5 and 9.3 MPa.<sup>47</sup> The compressive strength of the scaffolds was approximately 1.79–1.93 MPa, as shown in Table 2.

Although these scaffolds demonstrate mechanical properties similar to those of trabecular bone, their clinical application only becomes meaningful when combined with sufficient porosity to allow cellular infiltration, product exchange, and vascular growth.<sup>48</sup> The results (Figure 4B,C) reveal pore diameters ranging from approximately 150 to 0.06  $\mu\text{m}$ , this range of pore diameters is divided into inter- and intraporosity (Table 2). The porosity for W-P6-li is 20.8%, for W-0 it is 25.6%, and for W-05 it is 30.4%. The evolution of the porosity can be justified on the basis that W-P6-Li is a ceramic structure (W), characterized by being coated with a glassy phase (P6-Li). Consequently, the interparticle porosity is the lowest at 9.38%. This is because of the fact that the glass provides cohesion between the grains, thereby reducing the interparticle porosity. Subsequently, the aforementioned structure was coated with an undoped wollastonite ceramic (W-0), resulting in the generation of a granular structure and an increase in interparticle porosity (18.11%). When the coating was doped with Mg, a slight increase in the size of the porosity (27.13%) was observed. However, both scaffolds remained within the same range of interparticle porosity.

With regard to the intraparticle porosity, the application of successive coatings involving thermal treatments has been observed to result in a notable densification of the structure. This is evidenced by a reduction in the intraparticle porosity, obtaining values of 11.38% for W-P6-Li and in the range of 7.47–3.24% for W-0 and W-05, respectively.

One of the objectives of this research was to modulate the morphology of the precipitated HA-like in the *in vitro* tests by doping the outer coating with  $\text{Na}^+$ ,  $\text{K}^+$ , and  $\text{Mg}^{2+}$  ions. Upon exposure to SBF, these ions are released into the solution and can be incorporated into the precipitated HA-like. The integration of ions into the crystal lattice of apatites is extensively documented in scientific literature.<sup>49–52</sup> This mineral group has a loose structure that allows the inclusion of non-lattice atoms or particles substituting for  $\text{Ca}^{2+}$  and  $\text{PO}_4^{3-}$ .<sup>49,50,53</sup> The accumulation of these ion substitutions induces lattice distortions, which explains why the crystallinity of ion-doped HA is usually, but not always, lower than that of its pure counterpart.<sup>49,52</sup>

The presence of ions such as Mg, which have a higher volumetric charge density than  $\text{Ca}^{2+}$ , can result in the phenomenon known as Ostwald ripening.<sup>54–56</sup> This process, which involves dissolution and recrystallisation, ultimately leads to the formation of hollow sphere. In the initial stages of the HA-like precipitation process, the HA-like contains a higher amount of  $\text{Mg}^{2+}$ , being in a less

crystalline form. As the precipitate develops, the concentration of  $\text{Mg}^{2+}$  in the solution will decrease, thereby increasing the crystallinity of the HA-like. The initial HA-like structure, with a high  $\text{Mg}^{2+}$  content, is stressed. The dissolution of this structure results in the formation of an HA-like hollow sphere, which is characterized by a reduction in stress. The evolution of this process is accelerated in confined areas such as crevices, due to the smaller volume of the dissolution that occurs in these spaces. An example of this can be seen in sample W-05-7D (Figure 5), where the needles are thinner and more crystalline as compared to the rest of the micrographs.

As mentioned earlier, these modifications in the unit cell are expected to induce morphological changes in the precipitated HA-like. Following this objective, the samples W-0, W-05 and W-075 were scanned for apatite-like precipitates by FESEM-EDX as the SBF soaking time increased (Figure 5).

Sample W-0 showed a trend of losing Si and gaining P over time, until reaching an almost stoichiometric HA-like on day 7. The high Si content detected at 14 days resulted in a Ca/P ratio of approximately 2.35. Since high ratios promote HA dissolution,<sup>49</sup> it is not unexpected that the precipitate began to dissolve and eventually disappeared at 21 days, giving way to CaP crystals. This theory was confirmed by ICP-OES (Figure 6A). The increasing P content of the precipitate until day 7 led to a decrease in the P concentration in the SBF. However, from day 14 onward, the dissolution of the precipitate resulted in an increase in the P concentration, which was observable until day 21.

As for scaffold W-05, it showed a very interesting surface morphology. This composition was not only bioactive on all days of the study, but also showed great morphological changes. The initial precipitate has a crystalline structure in the form of needles forming spheres, which could be considered typical. However, after 3 days, it adopts a square shape, which, contrary to the above, indicates a lower crystallinity. A plausible explanation for the decrease in crystallinity is ionic substitutions. Among the possible replacements that can occur in HA-like is the substitution of  $\text{PO}_4^{3-}$  tetrahedra by  $\text{SiO}_4^{4-}$  tetrahedra.<sup>49,52,57</sup> When this occurs, the crystal size is reduced and the grain structure of the material changes,<sup>21,52,57</sup> assuming a square shape as shown in Figure 5 (W-05-3D) and consistent with the results of the EDX analysis, which shows significant amounts of Si (Table S3). This is very interesting from a therapeutic point of view, since silicate groups in the calcium-phosphate system are associated with a significant increase in the rate of osteogenesis *in vivo* after implantation. Furthermore, it is known that bone tissue remodeling is approximately twice as fast in silica-rich HA as in silica-deficient HA.<sup>52,57</sup>



After 1 week in SBF, spheres of approximately 2–3  $\mu\text{m}$  appear, which are hollow. It is hypothesized that this phenomenon is the result of the dissolution process occurring at a faster rate in confined areas. As previously stated, these spheres were located in a crevice where the concentration of ions of high volumetric charge density, such as  $\text{Mg}^{2+}$ , is lower. As internal atomic mobility and reorganization reduce crystalline defects over time, the higher crystallinity of HA-like on day 7 compared to day 14 demonstrates the significant effect of ionic exposure on HA-like.

The ICP-OES results demonstrate a constant decrease of the P concentration in the SBF (Figure 6B), associated with apatite precipitation. This precipitate is shown in Figure 5 sample W-05, where a continue bioactivity over times is noticed.

With regards to scaffold W-075, CaP precipitates were observed after 1 and 3 days of immersion in SBF, but disappeared on days 7, 14 and 21. Similar to W-05-3D, a high Si content was detected on the precipitate on day 1, which modified the HA-like morphology by thickening it and reducing the size of the crystals.<sup>57</sup> Although the morphology of the precipitate is similar to that of W-05-7D, the spheres in this case are compact and lack the capacity for drug loading. On the third day, the Si content decreased, resulting in thinner and more crystalline HA needles. There was a decrease in P concentration in SBF on Days 1 and 3 (Figure 6C), which corresponds mainly to the deposition of HA-like. Conversely, on Days 7, 14 and 21, the precipitate dissolves and the phosphorus concentration increases. These results suggest the progressive dissolution of the scaffold. Initially, the sample is bioactive, followed by the detection of  $\beta$ -TCP (Figure 5-7D), the third layer of the scaffold. After 14 days (Figure 5-14D), pyrophosphate, the main component of the W-P6-Li core along with cristobalite, is observed on the surface. Between Day 7 and 14, there is a significant increase in lithium concentration (only present in P6) in the SBF, indicating core dissolution.

Although all scaffolds showed interesting behavior, scaffold W-05 stands out for its consistent bioactivity throughout the 21-day study period. Additionally, on the seventh day following immersion in SBF, the formation of hollow HA-like spheres is observed. The three-dimensional porous structure and biodegradability of HA-like hollow spheres make them an optimal vehicle for controlled drug release.<sup>58,59</sup> This discovery represents a remarkable therapeutic advantage, allowing the combination of tissue engineering with sustained drug release.

This involves the integration of a scaffold into the damaged area to facilitate the restoration of the structure and function of the damaged tissue, together with the action of bioactive molecules, such as drugs or growth factors,

which are released directly at the target site. This in turn avoids side effects due to systemic distribution or first-pass hepatic metabolism, allowing the dose administered to be reduced.<sup>58</sup> Given all these advantages, the combination of scaffolds for tissue engineering and drug delivery has been the subject of intense research in recent years.<sup>60–62</sup>

In this sense, the MTT cell viability assay was performed on 3T3 fibroblasts exposed to the W-05 scaffold (direct assay) and its DP (indirect assay). This was done not only to assess the potential cytotoxicity of the samples, but also to determine whether variations in the surface morphology of the W-05 scaffold exhibited biologically enhanced properties.

In the direct assay (Figure 7A), lower cell proliferation was observed in fibroblasts seeded on the scaffolds compared to the control group cultured on plastic during the first 48 h. However, these differences disappeared by 72 h, indicating that the scaffolds are biocompatible. Furthermore, when comparing the different scaffolds, higher cell growth was observed on scaffold W-05-7D, which even exceeded that of the control group after 72 hours. These results suggest that surface morphology, based on hollow HA spheres, induces greater cell proliferation. This behavior has already been described by other authors. Jun Ji et al. fabricated nano-HA/chitosan/gelatin (nHA/CG) scaffolds with rod-nHA and sphere-nHA particles and found that sphere-nHA/CG significantly enhanced the proliferation and osteogenic differentiation of hiPSCs from hGF in vitro.<sup>63</sup> In particular, the cell number in sphere-nHA/CG was almost twice as high as in rod-nHA/CG after 12 weeks.

The results of the indirect assay showed higher cell viability in the wells containing DP-3D and DP-7D. While this difference was more pronounced for the 15 mg/mL concentration (Figure 7B), a very similar trend is observed for the 30 mg/mL concentration (Figure 7C). These results are very encouraging as they indicate that the degradation products are not only nontoxic but also cell division inducing.

## 5 | CONCLUSIONS



In this research work, innovative multilayer glass–ceramic scaffolds, with surface morphology modulation, have been developed for BTE through the application of the sol–gel method. The scaffolds' core, composed mainly of silicon dioxide, calcium pyrophosphate, and the vitreous phase P6-Li, provides mechanical strength comparable to that of cancellous bone. This characteristic, combined with a total porosity of the complete scaffolds over 87%, provides an environment conducive to cell infiltration and other physiological processes, making them suitable for load bearing applications.

Concerning the bioactive coatings, the outer layer modulates the morphological and bioactive behavior of the scaffolds through ion doping. Scaffold W-05, in particular, presented a surface covered by hollow HA spheres after 1 week of immersion in SBF, demonstrating its potential as an agent for controlled drug release. Additionally, this scaffold proved to be biocompatible, showing no evidence of toxicity on cells, either through direct contact or mediated by its dissolution products. Notably, the hollow spheres of W-05-7D were found to stimulate cell proliferation compared to the other scaffolds and the control. Additionally, the dissolution products of W-05 were found to increase cell viability compared to the control. These results suggest the potential for combining tissue engineering and drug delivery to provide significant therapeutic benefits while promoting bone regeneration.

## ACKNOWLEDGMENTS

This work is part of the project PID2020-116693RB-C21, funded by MCIN/AEI/10.13039/501100011033 Spain. In addition, P. M. Riosalido has received a grant PID2020-116693RB-C21 funded by the Generalitat Valenciana Spain. We are sincerely grateful for the valuable technical support provided by M. Desiree González Gras during the conduct of cellular studies.

## ORCID

Pablo Velásquez  <https://orcid.org/0000-0002-5142-4992>  
Piedad N. De Aza  <https://orcid.org/0000-0001-9316-4407>

## REFERENCES

- Malliappan SP, Yetisgin AA, Sahin SB, Demir E, Cetinel S. Bone tissue engineering: anionic polysaccharides as promising scaffolds. *Carbohydr Polym.* 2022;283. <https://doi.org/10.1016/j.carbpol.2022.119142>
- Tsiklin IL, Shabunin Av, Kolsanov Av, Volova LT. In vivo bone tissue engineering strategies: advances and prospects. *Polymers.* 2022;14(15). <https://doi.org/10.3390/polym14153222>
- Fu R, Liu C, Yan Y, Li Q, Huang RL. Bone defect reconstruction via endochondral ossification: a developmental engineering strategy. *J Tissue Engg.* 2021;12. <https://doi.org/10.1177/20417314211004211>
- Zhang Y, Wu D, Zhao X, Pakvasa M, Tucker AB, Luo H, et al. Stem cell-friendly scaffold biomaterials: applications for bone tissue engineering and regenerative medicine. *Front Bioeng Biotechnol.* 2020;8. <https://doi.org/10.3389/fbioe.2020.598607>
- Perić Kačarević Ž, Rider P, Alkildani S, Retnasingh S, Pejakić M, Schnettler R, et al. An introduction to bone tissue engineering. *Int J Artif Organs.* 2020;43(2). <https://doi.org/10.1177/0391398819876286>
- Kim HD, Amirthalingam S, Kim SL, Lee SS, Rangasamy J, Hwang NS. Biomimetic materials and fabrication approaches for bone tissue engineering. *Adv Healthc Mater.* 2017;6(23). <https://doi.org/10.1002/adhm.201700612>
- Turnbull G, Clarke J, Picard F, Riches P, Jia L, Han F, et al. 3D bioactive composite scaffolds for bone tissue engineering. *Bioact Mater.* 2018;3(3). <https://doi.org/10.1016/j.bioactmat.2017.10.001>
- Wubneh A, Tsekoura EK, Ayranci C, Uludağ H. Current state of fabrication technologies and materials for bone tissue engineering. *Acta Biomater.* 2018;80. <https://doi.org/10.1016/j.actbio.2018.09.031>
- Ribas RG, Schatkoski VM, Montanheiro TL, do A, de Menezes BRC, Stegemann C, et al. Current advances in bone tissue engineering concerning ceramic and bioglass scaffolds: a review. *Ceram Int.* 2019;45(17). <https://doi.org/10.1016/j.ceramint.2019.07.096>
- Pina S, Rebelo R, Correló VM, Oliveira JM, Reis RL. Bioceramics for osteochondral tissue engineering and regeneration. *Adv Exp Med Biol.* 2018;1058. [https://doi.org/10.1007/978-3-319-76711-6\\_3](https://doi.org/10.1007/978-3-319-76711-6_3)
- Baino F, Novajra G, Vitale-Brovarone C. Bioceramics and scaffolds: a winning combination for tissue engineering. *Front Bioeng Biotechnol.* 2015;3. <https://doi.org/10.3389/fbioe.2015.00202>
- Stastny P, Sedlacek R, Suchy T, Lukasova V, Rampichova M, Trunc M. Structure degradation and strength changes of sintered calcium phosphate bone scaffolds with different phase structures during simulated biodegradation in vitro. *Mater Sci Eng, C.* 2019;100. <https://doi.org/10.1016/j.msec.2019.03.027>
- Xiao D, Zhang J, Zhang C, Barbieri D, Yuan H, Moroni L, et al. The role of calcium phosphate surface structure in osteogenesis and the mechanisms involved. *Acta Biomater.* 2020;106. <https://doi.org/10.1016/j.actbio.2019.12.034>
- Denry I, Kuhn LT. Design and characterization of calcium phosphate ceramic scaffolds for bone tissue engineering. *Dent Mater.* 2016;32(1). <https://doi.org/10.1016/j.dental.2015.09.008>
- Kang HJ, Makkar P, Padalhin AR, Lee GH, Im S-B, Lee BT. Comparative study on biodegradation and biocompatibility of multichannel calcium phosphate based bone substitutes. *Mater Sci Eng, C.* 2020;110. <https://doi.org/10.1016/j.msec.2020.110694>
- Liao F, Peng XY, Yang F, Ke QF, Zhu ZH, Guo YP. Gadolinium-doped mesoporous calcium silicate/chitosan scaffolds enhanced bone regeneration ability. *Mater Sci Eng, C.* 2019;104:109999. <https://doi.org/10.1016/j.msec.2019.109999>
- Xin X, Wu J, Zheng A, Jiao D, Liu Y, Cao L, et al. Delivery vehicle of muscle-derived irisin based on silk/calcium silicate/sodium alginate composite scaffold for bone regeneration. *Int J Nanomedicine.* 2019;14:1451-67. <https://doi.org/10.2147/IJN.S193544>
- Ros-Tárraga P, Murciano Á, Mazón P, Gehrke SA, de Aza PN. In vitro behaviour of sol-gel interconnected porous scaffolds of doped wollastonite. *Ceram Int.* 2017;43(14):11034-38. <https://doi.org/10.1016/j.ceramint.2017.05.146>
- Ghamor-Amegavi EP, Yang X, Qiu J, Xie L, Pan Z, Wang J, et al. Composition control in biphasic silicate microspheres on stimulating new bone regeneration and repair of osteoporotic femoral bone defect. *J Biomed Mater Res B Appl Biomater.* 2020;108(2):377-90. <https://doi.org/10.1002/jbm.b.34396>
- Zenebe CG. A review on the role of wollastonite biomaterial in bone tissue engineering. *Biomed Res Int.* 2022;2022. <https://doi.org/10.1155/2022/4996530>
- Zhou X, Zhang N, Mankoci S, Sahai N. Silicates in orthopedics and bone tissue engineering materials. *J Biomed Mater Res—Part A.* 2017;105(7). <https://doi.org/10.1002/jbm.a.36061>

22. Truong LB, Medina Cruz D, Mostafavi E, O'connell CP, Webster TJ. Advances in 3d-printed surface-modified ca-si bioceramic structures and their potential for bone tumor therapy. *Materials*. 2021;14(14). <https://doi.org/10.3390/ma14143844>
23. Jafari N, Habashi MS, Hashemi A, Shirazi R, Tanideh N, Tamadon A. Application of bioactive glasses in various dental fields. *Biomater Res*. 2022;26(1). <https://doi.org/10.1186/s40824-022-00274-6>
24. Kaou MH, Furkó M, Balázi K, Balázi C. Advanced bioactive glasses: the newest achievements and breakthroughs in the area. *Nanomaterials*. 2023;13(16):2287. <https://doi.org/10.3390/nano13162287>
25. Montazeri M, Karbasi S, Foroughi MR, Monshi A, Ebrahimi-Kahrizsangi R. Evaluation of mechanical property and bioactivity of nano-bioglass 45S5 scaffold coated with poly-3-hydroxybutyrate. *J Mater Sci: Mater Med*. 2015;26(2):62. <https://doi.org/10.1007/s10856-014-5369-z>
26. Pantulap U, Arango-Ospina M, Boccaccini AR. Bioactive glasses incorporating less-common ions to improve biological and physical properties. *J Mater Sci: Mater Med*. 2022;33(1). <https://doi.org/10.1007/s10856-021-06626-3>
27. Parvizifard M, Karbasi S. Physical, mechanical and biological performance of PHB-Chitosan/MWCNTs nanocomposite coating deposited on bioglass based scaffold: potential application in bone tissue engineering. *Int J Biol Macromol*. 2020;152. <https://doi.org/10.1016/j.ijbiomac.2020.02.266>
28. Mata NA, Ros-Tárraga P, Velasquez P, Murciano A, de Aza PN. 3D multiphasic porous scaffolds of calcium phosphates doping with silicon and magnesium. *Bol Soc Esp Ceram Vidrio*. 2022;61(5). <https://doi.org/10.1016/j.bsecv.2021.03.004>
29. Ding S, Li L, Liu X, Yang G, Zhou G, Zhou S. A nano-micro alternating multilayer scaffold loading with rBMSCs and BMP-2 for bone tissue engineering. *Colloids Surf B*. 2015;133. <https://doi.org/10.1016/j.colsurfb.2015.06.015>
30. Sebastián E, Murciano A, Madrigal R, de Aza PN, Velasquez P. 3D CaP porous scaffolds with grooved surface topography obtained by the sol-gel method. *Ceram Int*. 2021;47(15). <https://doi.org/10.1016/j.ceramint.2021.04.158>
31. Miri Z, Haugen HJ, Loca D, Rossi F, Perale G, Moghanian A, et al. Review on the strategies to improve the mechanical strength of highly porous bone bioceramic scaffolds. *J Eur Ceram Soc*. 2024;44(1). <https://doi.org/10.1016/j.jeurceramsoc.2023.09.003>
32. Vahabzadeh S, Hack VK, Bose S. Lithium-doped  $\beta$ -tricalcium phosphate: effects on physical, mechanical and in vitro osteoblast cell-material interactions. *Biomed Mater Res B Appl Biomater*. 2017;105(2):391-9. <https://doi.org/10.1002/jbm.b.33485>
33. Hannon MJ, Verbalis JG. Sodium homeostasis and bone. *Curr Opin Nephrol Hypertens*. 2014;23(4). <https://doi.org/10.1097/01.mnh.0000447022.51722.f4>
34. Ha J, Kim SA, Lim K, Shin S. The association of potassium intake with bone mineral density and the prevalence of osteoporosis among older Korean adults. *Nut Res Pract*. 2020;14(1). <https://doi.org/10.4162/nrp.2020.14.1.55>
35. Rondanelli M, Faliva MA, Tartara A, Gasparri C, Perna S, Infantino V, et al. An update on magnesium and bone health. *Biometals*. 2021;34(4). <https://doi.org/10.1007/s10534-021-00305-0>
36. ISO/FDIS 23317 standard Implants for surgery- in vitro evaluation for apatite-forming ability of implant. <https://www.iso.org/standard/36406.html>
37. ISO 10993-5 Biological evaluation of medical devices Part 5: Tests for in vitro cytotoxicity. <https://www.iso.org/standard/36406.html>
38. Pasteris JD, Wopenka B, Valsami-Jones E. Bone and tooth mineralization: why apatite? *Elements*. 2008;4(2). <https://doi.org/10.2113/GSELEMENTS.4.2.97>
39. Fernández-Hernán JP, Torres B, López AJ, Rams J. The role of the sol-gel synthesis process in the biomedical field and its use to enhance the performance of bioabsorbable magnesium implants. *Gels*. 2022;8(7). <https://doi.org/10.3390/gels8070426>
40. Stachel D, Paulus H, Svoboda I, Fuess H. Crystal structure of calcium ultraphosphate,  $\text{Ca}_2\text{P}_6\text{O}_{17}$ . *Zeitschrift für Kristallographie*. 1992;202(1-2) 117-8. <https://doi.org/10.1524/zkri.1992.202.1-2.117>
41. Putra NE, Borg KGN, Diaz-Payno PJ, Leeflang MA, Klimopoulou M, Taheri P, et al. Additive manufacturing of bioactive and biodegradable porous iron-akermanite composites for bone regeneration. *Acta Biomater*. 2022;148. <https://doi.org/10.1016/j.actbio.2022.06.009>
42. Dong X, Li H, Lingling E, Cao J, Guo B. Bioceramic akermanite enhanced vascularization and osteogenic differentiation of human induced pluripotent stem cells in 3D scaffolds: in vitro and vivo. *RSC Adv*. 2019;9(44). <https://doi.org/10.1039/c9ra02026h>
43. Lee WB, Wang C, Lee JH, Jeong KJ, Jang YS, Park JY, et al. Whitlockite granules on bone regeneration in defect of rat calvaria. *ACS Applied Bio Materials*. 2020;3(11). <https://doi.org/10.1021/acsabm.0c00960>
44. Kazakova G, Safronova T, Golubchikov D, Shevtsova O, Rau Jv. Resorbable  $\text{Mg}^{2+}$ -containing phosphates for bone tissue repair. *Materials*. 2021;14(17). <https://doi.org/10.3390/ma14174857>
45. Kim HD, Jang HL, Ahn HY, Lee HK, Park J, Lee E-s, et al. Biomimetic whitlockite inorganic nanoparticles-mediated in situ remodeling and rapid bone regeneration. *Biomaterials*. 2017;112. <https://doi.org/10.1016/j.biomaterials.2016.10.009>
46. Zhou D, Qi C, Chen YX, Zhu YJ, Sun TW, Chen F, et al. Comparative study of porous hydroxyapatite/chitosan and whitlockite/chitosan scaffolds for bone regeneration in calvarial defects. *Int J Nanomed*. 2017;12:2673-87. <https://doi.org/10.2147/IJN.S131251>
47. Caeiro JR, González P, Guede D. Biomechanics and bone (& II): trials in different hierarchical levels of bone and alternative tools for the determination of bone strength. *Revista de Osteoporosis y Metabolismo Mineral*. 2013;5(2).
48. Codrea CI, Croitoru AM, Baciuc CC, Melinescu A, Ficai D, Fruth V, et al. Advances in osteoporotic bone tissue engineering. *J Clin Med*. 2021;10(2). <https://doi.org/10.3390/jcm10020253>
49. Pupilli F, Ruffini A, Dapporto M, Tavoni M, Tampieri A, Sprio S. Design strategies and biomimetic approaches for calcium phosphate scaffolds in bone tissue regeneration. *Biomimetics*. 2022;7(3). <https://doi.org/10.3390/biomimetics7030112>
50. Ratnayake JTB, Mucalo M, Dias GJ. Substituted hydroxyapatites for bone regeneration: a review of current trends. *J Biomed Mater Res B Appl Biomater*. 2017;105(5):1285-99. <https://doi.org/10.1002/jbm.b.33651>



51. Radulescu DE, Vasile OR, Andronescu E, Fikai A. Latest research of doped hydroxyapatite for bone tissue engineering. *Int J Mol Sci*. 2023;24(17). <https://doi.org/10.3390/ijms241713157>
52. Szurkowska K, Kolmas J. Hydroxyapatites enriched in silicon—bioceramic materials for biomedical and pharmaceutical applications. *Progress Nat Sci Mater Int*. 2017;27(4). <https://doi.org/10.1016/j.pnsc.2017.08.009>
53. Vranceanu DM, Ionescu IC, Ungureanu E, Cojocaru MO, Vladescu A, Cotrut CM. Magnesium doped hydroxyapatite-based coatings obtained by pulsed galvanostatic electrochemical deposition with adjustable electrochemical behavior. *Coatings*. 2020;10(8). <https://doi.org/10.3390/COATINGS10080727>
54. Wen-shou W, Cheng-Yan X., Li Y, Wen-Zhu S. Controlled synthesis of calcium tungstate hollow microspheres via ostwald ripening and their photoluminescence property. *J Phys Chem C*. 2008;112:19390–18. <https://doi.org/10.1021/jp8074783>
55. Jiang SD, Yao QZ, Zhou GT, Fu SQ. Fabrication of hydroxyapatite hierarchical hollow microspheres and potential application in water treatment. *J Phys Chem C*. 2012;116:4484–92, <https://doi.org/10.1021/jp211648x>
56. Sebastian E, Murciano A, De Aza PN, Velasquez P. Synthesis of 3D porous ceramic scaffolds obtained by the sol-gel method with surface morphology modified by hollow spheres for bone tissue engineering applications, *Ceram Inter*. 2023;49:4393–402. <https://doi.org/10.1016/j.ceramint.2022.09.326>
57. Lyutova E, Borilo L, Izosimova E. The effect of sodium and magnesium ions on the properties of calcium–phosphate biomaterials. *Progress Biomater*. 2019;8(2). <https://doi.org/10.1007/s40204-019-0117-6>
58. Halim NAA, Hussein MZ, Kandar MK. Nanomaterials-upconverted hydroxyapatite for bone tissue engineering and a platform for drug delivery. *Int J Nanomed*. 2021;16. <https://doi.org/10.2147/IJN.S298936>
59. Lara-Ochoa S, Ortega-Lara W, Guerrero-Beltrán CE. Hydroxyapatite nanoparticles in drug delivery: physicochemistry and applications. *Pharmaceutics*. 2021;13(10). <https://doi.org/10.3390/pharmaceutics13101642>
60. Mahanta AK, Senapati S, Paliwal P, Krishnamurthy S, Hemalatha S, Maiti P. Nanoparticle-induced controlled drug delivery using chitosan-based hydrogel and scaffold: application to bone regeneration. *Mol Pharmaceutics*. 2019;16(1). <https://doi.org/10.1021/acs.molpharmaceut.8b00995>
61. Chen C, Huang K, Zhu J, Bi Y, Wang L, Jiang J, et al. A novel elastic and controlled-release poly(ether-ester-urethane)urea scaffold for cartilage regeneration. *J Mater Chem B*. 2020;8(18). <https://doi.org/10.1039/c9tb02754h>
62. Ji J, Tong X, Huang X, Wang T, Lin Z, Cao Y, et al. Sphere-shaped nano-hydroxyapatite/chitosan/gelatin 3D porous scaffolds increase proliferation and osteogenic differentiation of human induced pluripotent stem cells from gingival fibroblasts. *Biomed Mater (Bristol)*. 2015;10(4). <https://doi.org/10.1088/1748-6041/10/4/045005>
63. Qin X, Wu Y, Liu S, Yang L, Yuan H, Cai S, et al. Surface modification of polycaprolactone scaffold with improved biocompatibility and controlled growth factor release for enhanced stem cell differentiation. *Front Bioeng Biotechnol*. 2022;9. <https://doi.org/10.3389/fbioe.2021.802311>

## SUPPORTING INFORMATION

Additional supporting information can be found online in the Supporting Information section at the end of this article.

**How to cite this article:** Riosalido PM, Velásquez P, Murciano Á, De Aza PN. Surface morphology modulation in multilayer scaffolds via ion doping for bone tissue engineering. *J Am Ceram Soc*. 2024;e20269. <https://doi.org/10.1111/jace.20269>